CCS Chemistry

IMMEDIATE ONLINE ACCEPTED (IOA) ARTICLE

IOA Posting Date: May 18, 2024

TITLE: The synergetic effect of dual active sites in ZnO-ZrO_2 catalyst for CO_2 hydrogenation to methanol

AUTHORS: Jijie Wang, Shunning Li, Wei Liu, Yinguo Xiao, Zhendong Feng, Xianhui Liang, Shan Tang, Guanna Li, Cheng Dong, Feng Pan, Can Li

DOI: 10.31635/ccschem.024.202404243

CITE THIS: *CCS Chem.* **2024**, Just Accepted. DOI: 10.31635/ccschem.024.202404243

The synergetic effect of dual active sites in ZnO-ZrO_2 catalyst for CO_2 hydrogenation to methanol

Jijie Wang[1†], Shunning Li[2†], Wei Liu[1†], Yinguo Xiao[2], Zhendong Feng[1,3], Xianhui Liang[2], Shan Tang[1,3], Guanna Li[4], Cheng Dong[2], Feng Pan[2*], Can Li[1,3*]

[1] State Key Laboratory of Catalysis, Dalian Institute of Chemical Physics, Chinese Academy of Sciences.

[2] School of Advanced Materials, Peking University Shenzhen Graduate School.

[3] University of Chinese Academy of Sciences.

[4] Biobased Chemistry and Technology, Wageningen University & Research.

†These authors contributed equally to this work.

*Corresponding author. Email: panfeng@pkusz.edu.cn, canli@dicp.ac.cn

Abstract

The reaction of CO_2 hydrogenation to methanol is a typical reaction requiring simultaneous activation of CO_2 and H_2. ZnO-ZrO_2 solid solution catalyst has been demonstrated to be an excellent catalyst and the dual active site of Zn-O-Zr was seen a key active site. However, it is not clear the actual surface configuration of Zn and Zr and how CO_2 and H_2 are activated on the active sites. Here, our research shows that there is a synergetic effect of dual active sites in ZnO-ZrO_2 catalyst for CO_2 hydrogenation to methanol. The main coordination form of 5%ZnO-ZrO_2 catalyst with low density of Zn-O-Zr site is isolated Zn site. The main coordination form of 20%ZnO-ZrO_2 catalyst with moderate density of Zn-O-Zr site is (Zn)-O-Zr-O-(Zn) site. The main coordination form of

40%ZnO-ZrO_2 catalyst with high density of Zn-O-Zr site is (Zn)-O-(Zn) site. The catalyst with modearte density of Zn-O-Zr site exhibits more efficient activation of H_2 and CO_2, lower energy barrier for rate-determing step, and leading to the superior catalytic activity. This work discovers the synergetic effect of Zn-O-Zr sites in ZnO-ZrO_2 catalyst for CO_2 hydrogenation to methanol, and sheds light on the importance of active site synergetic effect on multi-site catalysts.

Keywords

CO2 hydrogenation, methanol synthesis, dual active sites, synergetic effect, ZnO-ZrO2 catalyst

Introduction

The hydrogenation of CO_2 with renewable H_2 produced by solar and wind power is not only one of the most effective solutions to achieve net-zero carbon commitments, but also important in both academic and industrial contexts as the means of synthesizing value-added chemicals. Among the hydrogenation products, methanol (CH_3OH) is for achieving methanol economy, [1] and is particularly desired due to its capability and use as an easily transportable fuel and a precursor for the production of olefins and aromatics. Therefore, the methanol produced by hydrogenation of CO_2 with renewable H_2 is called "Liquid Sunshine methanol". [2, 3] The conversion of CO_2 and H_2 to methanol requires simultaneous activation of both reactants on close vicinity sites. This requirement motivates the research efforts to pursue bifunctional active sites in heterogeneous catalysts, which can be rendered by solid solution formation. [4–7] Bifunctional active sites possess dual catalytic sites that can independently regulate two activation processes and accommodate different reaction intermediates, while at the same time they work in synergy to steer the reaction towards the targeted product. Despite the recognized importance of bifunctional active sites, elucidating the detailed bifunctional reaction mechanism remains a huge challenge due to the difficulties in characterizing the nanoscale regimes at the surfaces and building the correct atomic configurations that enable the excellent catalytic performance.

Aided by advanced characterization technologies and theoretical simulation, the above challenges have been partially met on the $Cu/ZnO/Al_2O_3$ catalyst, [8–13] which is a prototypical system for studying promotional interactions in CO_2/CO-to-methanol reaction. A conceptual picture of Zn incorporation at the surfaces of Cu nanoparticles emerged after extensive investigation on this catalyst, which revealed the synergy of bifunctional Cu-Zn sites and the essential role of Zn coverage at Cu metal surface in boosting the methanol synthesis activity. [10–13] However, the poor stability of Cu-based catalysts is still a substantial problem confronting their practical application. Moreover, it is hard to achieve both satisfactory selectivity and high stability on nearly all the recently proposed catalysts. [14–19] By comparison, $ZnO\text{-}ZrO_2$ solid solution is renowned for its capability to catalyze the CO_2-to-methanol reaction in a fixed bed reactor with exceptional selectivity and stability, [4] but current studies still fall short in understanding the underlying active site and reaction mechanism. The standing challenge resides in identifying the key catalytic sites on oxide surfaces, which are far more complex than those at metal alloy surfaces. Although it was assumed that Zn-Zr pair site bridged by O ion [20,21] or ZnO_x/ZrO_2 interface [22–25] is responsible for the catalytic performance, it cannot fully explain the observed trends of activity and selectivity as a function of Zn content. Given the recent success in industrial application of $ZnO\text{-}ZrO_2$ solid solution catalysts (Fig. S1), it is urgently required to unravel the local structure of their catalytic sites, which may give inspiration to the further development of existing oxide catalysts and the design of new ones.

Herein, we investigated the compositional dependence of catalytic sites on the surface structure of $ZnO\text{-}ZrO_2$ solid solution. Through an interplay of theory and *in-situ* experiments, we disclose that with the increase of Zn concentration in $ZnO\text{-}ZrO_2$ catalyst, the density of Zn-O-Zr site raises and the shows a synergetic effect between a Zn-O-Zr site and another Zn-O-Zr site. We set up a discriptor which called the link distance (LD) [26,27] between neighboring Zn ions at the surface to illustrate the active site density effect on the catalytic reaction, thus deciding the overall compositional trends of activity and selectivity. In particular, an appropriate value of 4 for LD (with 4 consecutive between the neighboring Zn ions), which corresponds to a configuration of (Zn)-O-Zr-O-(Zn), can result in much lower activation barrier than LD = 2 (corresponding to (Zn)-O-(Zn) configuration) and

LD ≥ 6 (approximated as an isolated Zn dopant). The evolution of this atomic-scale structure as a function of Zn content matches well with the observed activity/selectivity maximum at the compositions close to about 20% ZnO-ZrO_2 (Zn/(Zn+Zr) = 20%). This discovery could guide the way for further optimization of surface structure for metal oxide solid solution catalysts.

Experimental Methods

1. Catalyst preparation

A series of *x*%ZnO-ZrO_2 catalysts (*x*% represents molar percentage of Zn, metal base) were prepared by coprecipitation method. Here we take the 20%ZnO-ZrO_2 catalyst as a typical example to describe the synthesis procedures: 0.74 g Zn $(NO_3)_2{\cdot}6H_2O$ and 5.19 g Zr $(NO_3)_4{\cdot}5H_2O$ were dissolved in a flask by 100 mL deionized water. The precipitator of 100 mL aqueous solution of 2.38 g $(NH_4)_2CO_3$ was added into the aforementioned solution (at a flow rate of 3 mL/min) under vigorous stirring at 70 °C so as to form a precipitate. The suspension was continuously stirred for 2 h at 70 °C, followed by cooling down to room temperature and filtering, washing with deionized water 3 times. The filtered sample was dried at 110 °C for 4 h and calcined at 500 °C in static air for 3 h. Other *x*%ZnO-ZrO_2 catalysts were prepared following the same method. All catalysts were pressed, crushed, and sieved to the size of 40–80 mesh for the activity evaluation.

2. Catalyst evaluation

The activity tests of the catalysts for CO_2 hydrogenation to methanol were carried out in a tubular fixed-bed continuous-flow reactor equipped with gas chromatography (GC). All catalysts were pressed, crushed, and sieved to the size of 40–80 mesh for the activity evaluation. Before the reaction, the catalyst (0.1 g, diluted with 0.4 g quartz sand) was pretreated in a H_2 or N_2 stream (0.1 MPa and 20 mL/min) at given temperatures. The reaction was conducted under reaction conditions of 2.0~5.0 MPa, 200~400 °C, $V(H_2)/V(CO_2)/V(Ar)$ = 72/24/4, and *GHSV* = 6000~24000 mL/ (g h). The exit gas from the reactor was maintained at 150 °C and

immediately transported to the sampling valve of the GC (Agilent GC-7890B), which was equipped with thermal conductivity and flame ionization detectors. Propark N and 5A molecular sieves packed columns (2 m×1/8 inch, Agilent) were connected to TCD while TG-BOND-Q capillary columns were connected to FID. The packed columns were used for the analysis of CO_2, Ar, CO, and the capillary column (30 m×0.32 mm×10 μm, ThermoFisher) for hydrocarbons, alcohols, and other C-containing products. CO_2 conversion (denoted as *X* (CO_2)) and the carbon-based selectivity (denoted as *S*(product)) for the carbon-containing products, including methane, methanol, and dimethyl ether, were calculated with an internal normalization method. Space time yield of methanol was denoted as *STY*(CH_3OH). All data were collected in 3 h after the reaction started (unless otherwise specified).

Calculation of single pass *X* (CO_2), *S*(CH_3OH), *S*(CO), *STY*(CH_3OH)

$$X(CO_2)=\frac{f_{CO}A_{CO}+i(f_{CH_4}A_{CH_4}+f_{CH_3OH}A_{CH_3OH}+2f_{CH_3OCH_3}A_{CH_3OCH_3})}{f_{CO_2}A_{CO_2}+f_{CO}A_{CO}+i(f_{CH_4}A_{CH_4}+f_{CH_3OH}A_{CH_3OH}+2f_{CH_3OCH_3}A_{CH_3OCH_3})},\quad i=\frac{f_{CH_4-TCD}A_{CH_4-TCD}}{f_{CH_4-FID}A_{CH_4-FID}}$$

$$S(CH_3OH)=\frac{if_{CH_3OH}A_{CH_3OH}}{f_{CO}A_{CO}+i(f_{CH_4}A_{CH_4}+f_{CH_3OH}A_{CH_3OH}+2f_{CH_3OCH_3}A_{CH_3OCH_3})}$$

$$S(CO)=\frac{f_{CO}A_{CO}}{f_{CO}A_{CO}+i(f_{CH_4}A_{CH_4}+f_{CH_3OH}A_{CH_3OH}+2f_{CH_3OCH_3}A_{CH_3OCH_3})}$$

$$STY(CH_3OH)=\frac{GHSV}{22.4}\times V\%(CO_2)\times X(CO_2)\times S(CH_3OH)\times M_{CH_3OH}$$

3. Catalyst characterization

(1) Powder X-Ray Diffraction (XRD)

The XRD results were collected on a Philips PW1050/81 diffractometer operating in Bragg-Brentano focusing geometry and using CuKα radiation (λ = 1.5418 Å) from a generator operating at 40 kV and 30 mA.

(2) High Resolution Transmission Electron Microscopy (HRTEM)

HRTEM images were obtained with a JEM-2100 microscope, 200 kV. The samples were prepared by placing a drop of nanoparticle ethanol suspension onto a lacey support film and allowing the solvent to evaporate.

(3) Neutron diffraction

The Neutron powder diffraction experiments were performed on a time-of-flight (TOF) neutron diffractometer, general purpose powder diffractometer (GPPD), at the China Spallation Neutron Source (CSNS). Each powder sample was loaded into a vanadium can with 9.1 mm in diameter and the neutron powder diffraction patterns were collected at room temperature with wavelength ranging from 0.1 Å to 4.9 Å. The neutron diffraction patterns were analyzed with the Rietveld refinement method by using the FullProf program.

(4) Aberration-corrected scanning transmission electron microscopy

The aberration-corrected scanning transmission electron microscopy (AC-STEM) was obtained on the JEM-ARM300F microscope with image and probe correctors. Specifically, to ensure the best satisfaction of non-coherent Z-contrast imaging the experiment was performed under 300kV to maximize the mean-free elastic scattering of incident electrons. High angle annular dark-field (HAADF) imaging was conducted using a 10-pA probe scanning at a convergence angle of 22 mrad and collection angle of 54-220 mrad simultaneously accompanied with collecting the annular bright-filed signal at around 10~22 mrad to visualize oxygen atoms in ZnO-ZrO_2 lattice. To reduce the risk of structural damage induced by high energy electron irradiation, the dose rate was kept below 6.8×10^3 $e \cdot Å^{-2} \cdot s^{-1}$ so as to achieve reliable atomic dopant information of zinc species embedding inside different ZrO_2 matrixes at varied dissolving concentrations. Elemental distribution analysis of ZnO-ZrO_2 samples was performed using a JED-2300T spectrometer (dual 165 mm^2 large area SDDs) equipped on ARM300F to obtain energy dispersive X-ray spectroscopy elemental mappings. Regarding the sample preparation, ZnO-ZrO_2 powders were dispersed in ethanol and subjected to ultrasonication for 10min followed

by placing a solution droplet of nanoparticle ethanol suspension onto a lacey support film and allowing the solvent to evaporate naturally.

(5) Extended X-ray absorption fine structure (EXAFS)

EXAFS fitting was performed using VIPER program. The fitting was performed alternatively in k and R spaces. When in the R space, it was done in the (Im + Module) mode, mathematically equivalent to the k-fit. The Fourier transformed (FT) data in R space were analyzed by applying ZnO and Zn foil Zn−O and Zn−Zn contributions.

(6) Inductively Coupled Plasma (ICP)

ICP experiment was performed using ICPS-8100 from Shimadzu with wavelength range 160 ~ 850nm and resolution 0.0045nm.

(7) Ex-situ X-ray Photoelectron Spectroscopy (XPS)

XPS was performed using a Thermo ESCALAB 250Xi with Al K radiation (15 kV, 10.8 mA, hν = 1486.6 eV) under ultrahigh vacuum (5×10^{-7} Pa), calibrated internally by the carbon deposit C(1s) (E_b = 284.6 eV). There is a sample cell that feed gas of CO_2 and H_2 can be induced into and can be heated at the same time.

(8) H_2-D_2 exchange experiment

H_2–D_2 exchange experiments were carried out in a flow reactor at 280 °C. The formation rate of HD was measured by mass signal intensity (ion current). 0.1 g sample was reduced with 10 mL/min H_2 at 280 °C for 1 h. Then, 10 mL/min D_2 was mixed with H_2 and together passed the catalyst sample. Reaction products HD, H_2 and D_2 were analysed with a mass spectrometer (GAM200, IPI). The m/z mass values used are 2 for H_2, 4 for D_2 and 3 for HD.

4. DFT calculation

All DFT calculations were performed using the Vienna Ab Initio Simulation Package (VASP). [28] The generalized gradient approximation (GGA) with PBE exchange and correlation functional was used to account for the exchange-correlation energy. [29] The kinetic energy cutoff of the plane wave basis set was set to 400 eV. A Gaussian smearing of the population of partial occupancies with a width of 0.1 eV was used. The threshold for energy convergence for each iteration was set to 10^{-5} eV. Geometry optimization was assumed to be converged when forces on each atom were less than 0.05 eV/Å. The minimum-energy reaction pathways and the corresponding transition states were determined using the climbing-image nudged-elastic band method (CI-NEB) implemented in VASP. [30] Frequency analysis was performed by means of the finite difference method as implemented in VASP. Each transition state was confirmed by the presence of a single imaginary frequency corresponding to the specific reaction path.

The optimized lattice parameters for tetragonal ZrO_2 bulk are a = b = 3.684 Å and c = 5.222 Å, which are in good agreement with the experimental values of a = b = 3.612 Å and c = 5.212 Å. [31] Defect energy was defined as $E_d = E_{substitute+vacancy} - E_{pristine} + E_{ZrO2} - E_{ZnO}$, where $E_{substitute+vacancy}$ is the energy of a ZrO_2 supercell with a Zn_{Zr} substitutional dopant and an oxygen vacancy, $E_{pristine}$ is the energy of a pristine ZrO_2 supercell, E_{ZrO2} is the energy of ZrO_2 per formular unit, and E_{ZnO} is the energy of ZnO per formular unit. The most stable (101) surface of ZrO_2 tetragonal phase was simulated by a 2×3×1 supercell slab model including four ZrO_2 sub-layers, each including two oxygen atomic layers and one Zr atomic layer. The ZrO_2 slab was separated by a vacuum layer with a thickness of 15 Å along the surface normal direction to avoid spurious interactions between periodic slab models. To take into account the effect of Zn^{2+} doping, one of the Zr^{4+}-O^{2-} moiety on the surface was replaced by a Zn^{2+} cation and an oxygen vacancy (Zn^{2+}-V_O). The atoms of top two ZrO_2 sub-layers were fully optimized, while the other two ZrO_2 sub-layers at the bottom were fixed at their optimized bulk positions throughout the surface calculations. The on-site Coulomb correction for the Zr 4*d* states of ZrO_2 bulk as well as the surface was included by DFT+U approach with a U_{eff} value of 4.0 eV. K-point grids of 8×8×6 and 3×5×1 generated by

Monkhorst-Pack scheme were used for sampling the Brillouin zones of ZrO_2 bulk and Zn-ZrO_2 supercell surface slab model, respectively.

Free energy for surface adsorbates was defined as $G = E_{DFT} + E_{ZPE} - TS$, where E_{DFT} is DFT ground state energy, E_{ZPE} is zero-point energy, T is temperature and S is entropy. The vibrational frequencies of adsorbed species were calculated, from which the vibrational entropies (S_{vib}) and the zero-point energies (E_{ZPE}) in the Gibbs free energy were obtained within harmonic approximations using the finite difference method in VASP. For pure gas phase, entropy from all degrees of freedom (translation, rotation, and vibration) was taken into consideration according to the experimental data at 593 K. The activation energy of a chemical reaction was defined as the energy difference between the initial and transition states, while the reaction energy was defined as the energy difference between the initial and final states.

Results and Discussion

Structures of ZnO-ZrO_2 catalysts and catalytic performances

We prepare a series of ZnO-ZrO_2 catalysts by co-precipitation method with the optimized synthesis conditions provided in Supplementary Information. Refined neutron and X-ray diffraction patterns (Fig. 1A-B, Fig. S2 and Table S1) demonstrate that there are two phases in pure ZrO_2 at room temperature, monoclinic (majority) and tetragonal (minority). Introduction of Zn dopants ($x \geq 1\%$) induces a transition of the monoclinic phase into the tetragonal one, and all monoclinic phase is transformed into tetragonal one when x reaches 5%. Further increase in Zn content ($x \geq 33\%$) leads to phase transition from tetragonal to cubic, with the simultaneous emergence of hexagonal ZnO due to phase segregation. This result is affirmed by HRTEM in Fig. S3. We note that the transition from monoclinic to tetragonal, then to cubic is through slight displacive distortions and without long-range redistribution of atoms (Fig. 1E). This feature, along with the smooth and steady evolution of lattice parameters versus Zn content at $0 \leq x \leq 40\%$ (Fig. 1C), strongly supports the solid-solution structure model in this composition range, which is also confirmed by the results of refined X-ray patterns (Table S2).

Extended X-ray absorption fine structure (EXAFS) measurements (Fig. S4A) reveal that Zn-Zn and Zn-O-Zn shells are barely discernible at compositions before ZnO segregation, indicating that Zn atoms are dispersed as substitutional dopants to replace Zr in the ZrO_2 lattice.

The catalyst's actual elementary compositon and the surface elementary compositon were determined by Inductively Coupled Plasma (ICP) and X-ray photoelectron spectroscopy (XPS) respectively. The results demonstrate there is an enrichment phenomenon of Zn concentration at the catalyst surface (Fig. S5). For $x \geq$ 33%, a steep increase of Zn content is revealed according to the XPS spectra, indicating the partial coverage of ZnO on the surface of the solid solution particles. Because the valence state of Zn species is +2 (revealed by XANES in Fig. S4B), for charge neutrality, each Zn substitutional dopant in ZrO_2 will bring about the formation of a single O vacancy (V_O). Consistently, the XPS of V_O related content (Fig. S6) displays increasing and decreasing trends before and after x = 20%, respectively, thus substantiating the substitutional Zn_{Zr} solid solution model and the surface segregation of ZnO. By means of density functional theory (DFT), the formation energies of Zn_{Zr}-V_O defect complex in monoclinic, tetragonal and cubic ZrO_2 phases were calculated to be 3.38, 1.99 and 1.57 eV, respectively. This result implies that the energy compensation of Zn_{Zr}-V_O defect formation in structures with higher symmetry is the driving force for the phase transition of ZnO-ZrO_2 solid solution.

The catalytic performance of ZnO-ZrO_2 catalysts was investigated (in a fixed bed reactor under the conditions of H_2/CO_2=3, 24000 h^{-1}, 2 MPa, 300 ^oC, details provided in Supplementary Information). Methanol and CO are the main products. Figure 1D shows the CO_2 conversion rate and selectivity of methanol as a function of Zn content in the catalysts. As expected, both pure ZrO_2 and ZnO shows inferior catalytic performance, while the activity is significantly enhanced when the two components are chemically mixed. The volcano patterns of both activity and selectivity raise the hypothesis that the effective catalytic sites of ZnO-ZrO_2 catalysts could evolve depending on the Zn content at the surface. Especially, at bulk Zn contents between 5% and 40% where the tetragonal solid solution phase is predominating, the change in Zn coordination configurations could be the governing factor for rationalizing the observed volcano patterns near the optimal composition ($x \approx$ 20%).

Coordination configurations of catalysts near the surface.

X ray Energy-dispersive spectroscopy (EDS) analysis combined with aberration-corrected scanning transmission electron microscopy (STEM) imaging for 5%ZnO-ZrO_2, 20%ZnO-ZrO_2 and 40%ZnO-ZrO_2 samples (Fig. 2A) show that at low ZnO content (5% and 20%) all the elements of zinc, oxygen and zirconium in ZnO-ZrO_2 solid-solution catalysts are overall in homogenous distribution, in absence of obvious atomic aggregation. At higher Zn contents, two or more Zn_{Zr} could be in a close vicinity, which is fundamentally different from the case of isolated Zn_{Zr} centers. The pattern of Zn-Zr-Zn columns in a sequence, as evidenced in the HAADF image of 20% ZnO-ZrO_2 along the t-ZrO_2 <010> direction, indicates the coordination configuration of (Zn)-O-Zr-O-(Zn) (LD = 4, shown in Fig. 2B) in the surface region. Along with this configuration, we also identified configurations of isolated Zn (LD ≥ 6) and (Zn)-O-(Zn) (LD = 2), the latter corresponding to local concentrated Zn_{Zr} region emerged due to the random distribution of Zn dopants. As compared to the 20%ZnO-ZrO_2 sample, the 5%ZnO-ZrO_2 sample shows a relatively sparse distribution of Zn dopants (Fig. S7), with much less frequent appearance of the (Zn)-O-Zr-O-(Zn) configuration. For the 40%ZnO-ZrO_2, more (Zn)-O-(Zn) (LD = 2) configurations are observed, however there is no evidence to exclude the configurations of LD = 4 and LD ≥ 6.

To further depict the fine structure of ZnO-ZrO_2 surface with optimal catalytic performance, high-angle annular dark-field (HAADF) mode has been performed for the ZnO-ZrO_2 sample as shown in Fig. 2C. The projected contrast reveals that there are sparse sites of weak contrast located at very close distance to the lattice sites of Zr columns. Since in non-coherent scattering imaging, weak scattering contrast is attributed to the column composed of light atoms, these weak scattering sites are thus identified to be Zn dopants at Zr sites with a small distortion that brings Zn visible. Figure 2C directly shows the structural evidence for the three configurations.

In the annular bright-field (ABF) image, an abundance of surface V_O is shown embedded in a distinct area of high Zn content. The O/Zr ratio in the surface region (the outmost 3~4 atom layers) is slightly lower than that

in the bulk (Fig. S8), which is consistent with the XPS results showing the enrichment of Zn dopants at the surface induces enrichment of oxygen vacancy. Overall, the above atom-revolved microstructure analysis indicate that the coordination environment of metal ions at the surface is derived as a function of Zn content in the solid solution, and the LD between neighboring Zn dopants could serve as a critical factor governing the intrinsic properties of the surface coordination configurations.

Activation of CO_2 and H_2 on catalysts

We further investigated the activation of CO_2 and H_2 on the catalysts. The CO_2-temperature program desorption (TPD) results show that there are two desorption peaks for all catalysts: low temperature peak (below 340 °C) and high temperature peak (above 340 °C) (Fig. S9). The low temperature peak is more related to the CO_2 hydrogenation reaction since the reaction temperature is not higher than 320 °C. After the adsorption capacity is normalized by surface area (Table S3), it can be seen that ZrO_2 and ZnO adsorb similar amounts of CO_2 for the low temperature peak (Fig. 3A), while the 20%ZnO-ZrO_2 catalyst presents a much stronger ability in activating CO_2 than the others. This may be related to the basicity of metal oxide and the amounts of V_O on the surface.[32–34] In addition, CO_2 is activated by the oxide catalysts in the form of carbonate or hydrocarbonate species (Fig S10). The H_2 activation can be estimated by H_2–D_2 exchange reaction (Fig S11). Figure 3B shows that ZnO has a much stronger ability for H_2 activation than ZrO_2 per square meter, indicating the essential role of Zn sites in H_2 activation on the solid solution ZnO-ZrO_2 catalyst. The activity of 20%ZnO-ZrO_2 is greater than 5%ZnO-ZrO_2 and 40%ZnO-ZrO_2. The ability to activate hydrogen for each Zn atom has a distinct transition at 20% ZnO-ZrO_2. It can be inferred that the electronic property of Zn or Zr must be changed in ZnO-ZrO_2 solid solution. XPS (Fig. S12) show that the binding energies of Zn in 5-40%ZnO-ZrO_2 are lower than that in ZnO, while the binding energy of Zr in 50-80%ZnO-ZrO_2 are lower than that in ZrO_2. Therefore, it is suggested that property of Zn in ZrO_2-based solid solution is changed and the Zn site is responsible for activation of H_2.

DFT calculations

DFT calculations elucidate how the catalytic activity could be tuned by the surface local atomic configuration of ZnO-ZrO_2 catalysts. Figure 4A shows the random distribution of Zn and Zr at the (101) surface of the tetragonal phase. With increasing Zn content, the LD between each pair of nearest Zn atoms at the surface is reducing from predominantly 6 or higher to 4 and then to 2, and the atomic structures shown are adopted for the following calculations of coordination configurations representing isolated Zn, (Zn)-O-Zr-O-(Zn) and (Zn)-O-(Zn), respectively.

On the Zn-O site at the surface, H_2 molecule heterolytically dissociates into a H^- (bonded to Zn) and a H^+ (bonded to a neighboring O), as demonstrated from the charge density difference plot in Fig. 4B. This result holds regardless of the content of surface Zn, and suggests that the H^- attacks the carbon atom of adsorbed carbonate while the transfer of proton to the oxygen atom of the carbonate species is simultaneously accompanied (Fig. 4C). It is noted that the lowest unoccupied molecular orbital (LUMO) of CO_2 in the linear geometry is degenerate, which undergoes an orbital splitting upon molecular bending. [35] One of the orbitals drops in energy, providing the possibility for electron transfer during the first hydrogenation step of CO_2, where the H^- contributes to the formation of a C-H covalent bond. This scenario is substantiated by the fact that the H^- on Zn can facilitate the first hydrogenation step. In CO_2-to-methonal reaction (Fig. 4C), two main stages are involved: (i) CO_2 → HCOOH →H_2COOH*, in which the O-C-O moiety is highly bent (~127°), and (ii) H_2CO* → H_3COH*, where the O atom is attached to the surface. On the Zn-O site, H_2 dissociation is exothermic in free energy over a low energy barrier of 0.25 eV. In comparison, the energy consumption of H_2 dissociation on a Zr-O site is much higher (0.60 eV), and after dissociation, both H adatoms could readily recombine with an extremely low kinetic barrier (Fig. S13). Therefore, Zn atoms are indispensable not only for driving the phase transition of ZrO_2, but also for heterolytic cleavage of H_2 for the initiation reduction of CO_2.

We find that the formation of HCOO* intermediate generally exhibits a large energy release (Fig. 4D, Fig. S14-16). This highly exothermic step would likely give rise to a large energy uptake in one of the subsequent steps, since the overall reaction of CO_2 hydrogenation to methanol is endothermic. For the isolated Zn case (Fig. S17-19), the rate-determining step (RDS), i.e., the **7** → **8** step, which happens to be the transition point between two reaction processes, is characterized by a free-energy barrier of 1.40 eV. For (Zn)-O-(Zn) configuration (Fig. S20-22), the adsorption structures of all the intermediates bear a strong resemblance to those for isolated Zn, and therefore their energy profiles are quite similar. Yet, the barrier of RDS for (Zn)-O-(Zn) is slightly lower (1.36 eV), owing to the higher energy of the H_2COOH* configuration, where only one Zr-O bond exists between the intermediate and the catalytic center, as compared to two bonds on isolated Zn (Fig. S20 and S23). Interestingly, for (Zn)-O-Zr-O-(Zn) configuration, the **7** → **8** step can proceed with a remarkably low barrier, while the **5** → **6** step becomes the RDS, with an energy barrier of 0.90 eV. The high activity could be ascribed to the reduced stability of reaction intermediates **4** to **7**, which leads to an overall flattening of the energy profile. The (Zn)-O-Zr-O-(Zn) active site has the merit of possessing two Zn_{Zr} catalytic centers to guarantee ample sites for the accommodation of dissociated H. These features participate in the bifunctional mechanism, in which Zn dopants act as the H^- pumps and the confined domain of ZrO_2 between two Zn dopants serves as the effective site for CO_2 adsorption and subsequent CO_2 hydrogenation.

Surface species variation on catalysts

In-situ diffuse reflectance infrared Fourier transform spectroscopy (DRIFTS) results help provide more evidence for the above mechanistic insights (Fig. 5). The peaks at 2875 and 2819 cm^{-1} can be attributed to HCOO* (intermediate **4**) and H_3CO* (intermediate **11**) species, respectively (Fig. S23 and Table S4). [36-38] The strong intensity of these peaks indicates the high stability of both HCOO* and H_3CO*, in agreement with the fact that they are located at the valleys of the reaction energy profiles (Fig. 4D, Figs. S13, 16 and 19). The concentrations of both species reach a steady state after reaction. We note that the 20%ZnO-ZrO_2 sample exhibits higher concentrations of these intermediates than 5%ZnO-ZrO_2 and 40%ZnO-ZrO_2, which is consistent with the

superior catalytic activity of the former. The intensity of HCOO* decreases and the intensity of H_3CO* increases when the reaction gas switches to H_2 (Fig. 5A-C). This suggests the facile conversion of HCOO* to H_3CO* upon hydrogenation, thus justifying the format pathway of CO_2-to-methanol reaction as presented in the DFT calculations. Comparison of the increase rate of CH_3O* among three compositions (Fig. 5D) highlight the optimal conversion rate and methanol selectivity at x = 20%, which is in line with above experimental results.

Conclusion

using a combination of neutron diffraction, atomic-resolution microscopy, *in-situ* spectroscopy and theoretical modelling, we have identified the bifunctional surface active sites of ZnO-ZrO_2 solid solution catalysts and established the underlying relationship between the Zn-O-Zr site and catalytic performance. At the composition with optimal performance, i.e., ~20%ZnO-ZrO_2, the coordination configuration of (Zn)-O-Zr-O-(Zn) prevails at the catalyst surface and functions as the active sites for CO_2 hydrogenation to methanol. Zn dopants enable the dissociation of H_2 and facilitate the transfer of H^- ions to the reaction intermediates, while the confined domain of ZrO_2 between two Zn dopants yields a flattened energy landscape for the accommodation of the reaction intermediates. Their interplay steers the reaction towards methanol production, with a much lower activation barrier than isolated Zn sites and dinuclear Zn sites (in the configuration of (Zn)-O-(Zn)). Our findings have far-reaching implications for how the synergetic effect of dual active site in catalysts can be rationally designed to create effective bifunctional active sites for CO_2 hydrogenation to methanol.

Supporting Information

Supporting Information is avaliable and includes Figs. S1 to S23, Tables S1 to S4.

Conflict of Interest (required)

There is no conflict of interest to report.

Funding Information (required)

This work was supported by grants from the Fundamental Research Center of Artificial Photosynthesis (FReCAP, No. 22088102), National Natural Science Foundation of China (No. 22172160), Clean energy Pilot Project of CAS (XDA0400303) and Outstanding Member Youth Innovation Promotion Association CAS.

Acknowledgments (required, if applicable)

The authors thank Prof. R. Si for the help with the EXAFS measure and data analysis.

References

1. Olah, G. A. Beyond Oil and Gas: The Methanol Economy. *Angew. Chem. Int. Ed.* **2005**, *44*, 2636–2639.

2. Shih, C., Zhang, T., Li, J. and Bai, C. Powering the future with liquid sunshine. *Joule* **2018**, *2*, 1925–1949.

3. Wang J., Han Z., Chen S., et al. Liquid sunshine methano l[J]. *Chemical Industry and Engineering Progress*, **2022**, *41*, 1309–1317.

4. Wang, J., Li, G., Li, Z., Tang, C., Feng, Z., An, H., Liu, H., Liu, T. and Li, C. A highly selective and stable ZnO-ZrO_2 solid solution catalyst for CO_2 hydrogenation to methanol. *Sci. Adv.* **2017**, *3*, e1701290.

5. Wang, J., Tang, C., Li, G., Han, Z., Li, Z., Liu, H., Cheng, F. and Li, C. High-performance M_aZrOx (M_a=Cd, Ga) solid-solution catalysts for CO_2 hydrogenation to methanol. *ACS Catal.* **2019**, *9*, 10253–10259.

6. Han, Z., Tang, C., Sha, F., Tang, S., Wang, J. and Li, C. CO_2 hydrogenation to methanol on ZnO-ZrO_2 solid solution catalysts with ordered mesoporous structure. *J. Catal.* **2021**, *396*, 242–250.

7. Sha, F., Tang, C., Tang, S., Wang, Q., Han, Z., Wang, J. and Li, C. The promoting role of Ga in $ZnZrO_x$ solid solution catalyst for CO_2 hydrogenation to methanol. *J. Catal.* **2021**, *404*, 383–392.

8. Graciani, J., Mudiyanselage, K., Xu, F., Baber, A. E., Evans, J., Senanayake, S. D., Stacchiola, D. J., Liu, P., Hrbek, J., Sanz, J. F. et al. Highly active copper-ceria and copper-ceria-titania catalysts for methanol synthesis from CO_2. *Science* **2014**, *345*, 546–550.

9. Kondrat, S. A., Smith, P. J., Wells, P. P., Chater, P. A., Carter, J. H., Morgan, D. J., Fiordaliso, E. M., Wagner, J. B., Davies, T. E., Lu, L. et al.. Stable amorphous georgeite as a precursor to a high-activity catalyst. *Nature* **2016**, *531*, 83–87.

10. Behrens, M., Studt, F., Kasatkin, I., Kühl, S., Hävecker, M., Abild-Pedersen, F., Zander, S., Girgsdies, F., Kurr, P., Kniep B.-L. et al. The active site of methanol synthesis over $Cu/ZnO/Al_2O_3$ industrial catalysts. *Science* **2012**, *336*, 893–897.

11. Kuld, S., Thorhauge, M., Falsig, H., Elkjær, C. F., Helveg, S., Chorkendorff, I. and Sehested, J. Quantifying the promotion of Cu catalysts by ZnO for methanol synthesis. *Science* **2016**, *352*, 969–974.

12. Kattel, S., Ramirez, P. J., Chen, J. G., Rodriguez, J. A. and Liu, P. Active sites for CO_2 hydrogenation to methanol on Cu/ZnO catalysts. *Science* **2017**, *355*, 1296–1299.

13. Amann, P., Klötzer, B., Degerman, D., Köpfle, N., Götsch, T., Lömker, P., Rameshan, C., Ploner, K., Bikaljevic, D., Wang, H. et al. The state of zinc in methanol synthesis over a Zn/ZnO/Cu(211) model catalyst. *Science*, **2022**, *376*, 603–608.

14. Sun, K., Fan, Z., Ye, J., Yan, J., Ge, Q., Li, Y., He, W., Yang, W. and Liu, C. Hydrogenation of CO_2 to methanol over In_2O_3 catalyst. *J. CO_2 Util.* **2015**, *12*, 1–6.

15. Li, C., Melaet, G., Ralston, W. T., An, K., Brooks, C., Ye, Y., Liu, Y., Zhu, J., Guo, J., Alayoglu, S. and Somorjai, G. A. High-performance hybrid oxide catalyst of manganese and cobalt for low-pressure methanol synthesis. *Nat. Commun.* **2015**, *6:* 6538.

16. Wang, L., Guan, E., Wang, Y., Wang, L., Gong, Z., Cui, Y., Meng, X., Gates, B. C. and Xiao F. Silica accelerates the selective hydrogenation of CO_2 to methanol on cobalt catalysts. *Nat. Commun.* **2020**, 11: 1033.

17. Hu, J., Yu, L., Deng, J., Wang, Y., Cheng, K., Ma, C., Zhang, Q., Wen, W., Yu, S., Pan, Y. et al. Sulfur vacancy-rich MoS_2 as a catalyst for the hydrogenation of CO_2 to methanol. *Nat. Catal.* **2021**, *4*, 242–250.

18. Wang, J., Meeprasert, J., Han, Z., Wang, H., Feng, Z., Tang, C., Sha, F., Tang, S., Pidko, E. A. and Li, C. Highly dispersed Cd cluster supported on TiO_2 as an efficient catalyst for CO_2 hydrogenation to methanol. *Chin. J. Catal.* **2022**, *43*, 761–770.

19. Meng, C., Zhao, G., Shi, X., Chen, P., Liu, Y. and Lu, Y. (2021). Oxygen-deficient metal oxides supported nano-intermetallic $InNi_3C_{0.5}$ toward efficient CO_2 hydrogenation to methanol. *Sci Adv.* **2021**, *7*, eabi6012.

20. Zhang, J. An, B., Li, Z., Cao, Y., Dai, Y., Wang, W., Zeng, L., Lin, W. and Wang, C. Neighboring Zn−Zr sites in a metal−organic framework for CO_2 hydrogenation. *J. Am. Chem. Soc.* **2021**, *143*, 8829−8837.

21. Tada, S., Ochiai, N., Kinoshita, H., Yoshida, M., Shimada, N., Joutsuka, T., Nishijima, M., Honma, T., Yamauchi, N., Kobayashi, Y. et al. Active sites on $Zn_xZr_{1-x}O_{2-x}$ solid solution catalysts for CO_2-to-methanol hydrogenation. *ACS Catal.* **2022**, *12*, 7748–7759.

22. Temvuttirojn, C., Poo-arporn, Y., Chanlek, N., Cheng, C., Chong, C., Limtrakul, J. and Witoon, T. Role of calcination temperatures of ZrO_2 support on methanol synthesis from CO_2 hydrogenation at high reaction temperatures over ZnO_x/ZrO_2 catalysts. *Ind. Eng. Chem. Res.* **2020**, *59*, 5525–5535.

23. Zhang, J., An, B., Cao, Y., Li, Z., Chen, J., He, X. and Wang, C. ZnO Supported on a Zr-based metal–organic framework for selective CO_2 hydrogenation to methanol. *ACS Appl. Energy Mater.* **2021**, *4*, 13567–13574.

24. Lin, L., Wang, G. and Zhao, F. CO_2 hydrogenation to methanol on ZnO/ZrO_2 catalysts: effects of zirconia phase. *ChemistrySelect* **2021**, *6*, 2119–2125.

25. Salusso, D., Borfecchia, E. and Bordiga, S. Combining X-ray diffraction and X-ray absorption spectroscopy to unveil Zn local environment in Zn-doped ZrO_2 catalysts. *J. Phys. Chem. C* **2021**, *125*, 22249−22261.

26. Kuhn, F., Wattenhofer, R., Zhang, Y. and Zollinger, A. Geometric ad-hoc routing: of theory and practice. *Proceedings of the twenty-second annual symposium on Principles of distributed computing.* **2003**, *3*, 63−72.

27. Li, S., Chen, Z., Wang, Z., Weng, M., Li, J., Zhang, M., Lu, J., Xu, K. and Pan, F. Graph-based discovery and analysis of atomic-scale one-dimensional materials. *Natl. Sci. Rev.* **2022**, *9*, 6.

28. Kresse, G. and Furthmüller, J. Efficient iterative schemes for ab initio total-energy calculations using a plane-wave basis set. *Phys. Rev. B* **1996**, *54*, 11169–11186.

29. Perdew, J. P., Burke, K. and Ernzerhof M. Generalized gradient approximation made simple. *Phys. Rev. Lett.* **1997**, *78*, 1396.

30. Henkelman, G., Uberuaga, B. P. and Jonsson, H. A climbing image nudged elastic band method for finding saddle points and minimum energy paths. *J. Chem. Phys.* **2000**, *113*, 9901.

31. Igawa, N. and Ishii, Y. Crystal structure of metastable tetragonal zirconia up to 1473 K. *J. Am. Ceram. Soc.* **2001**. *84*, 1169–1171.

32. Ghuman, K. K., Hoch, L. B., Wood, T. E., Mims, C., Singh, C. V. and Ozin, G. A. Surface analogues of molecular frustrated lewis pairs in heterogeneous CO_2 hydrogenation catalysis. *ACS Catal.* **2016**, *6*, 5764−5770.

33. Yu, K., Lou, L., Liu, S. and Zhou, W. Asymmetric oxygen vacancies: the intrinsic redox active sites in metal oxide catalysts. *Adv. Sci.* **2020**, *7*, 1901970.

34. Cimino, A. and Stone, F. S. Oxide solid solutions as catalysts. *Adv. Catal.* **2002**, *47*, 141–306.

35. Freund, H. J. and Roberts, M. W. Surface chemistry of carbon dioxide. *Surf. Sci. Rep.* **1996**, 25, 225–273.

36. Fisher, I. A. and Bell, A. T. *In-situ* infrared study of methanol synthesis from H_2/CO_2 over Cu/SiO_2 and $Cu/ZrO_2/SiO_2$. *J. Catal.* **1997**, *172*, 222–237.

37. Kattel, S., Yan, B., Yang, Y., Chen, J. G. and Liu, P. Optimizing binding energies of key intermediates for CO_2 hydrogenation to methanol over oxide-supported copper. *J. Am. Chem. Soc.* **2016**, *138*, 12440–12450.

38. Feng Z., Tang C., Zhang P., Li K., Li G., Wang J., Feng Z., and Li C. Asymmetric Sites on the ZnZrOx Catalyst for Promoting Formate Formation and Transformation in CO_2 Hydrogenation. *J. Am. Chem. Soc.* **2023**, *145*, 23, 12663–12672

Table of Contents Graphic (required)

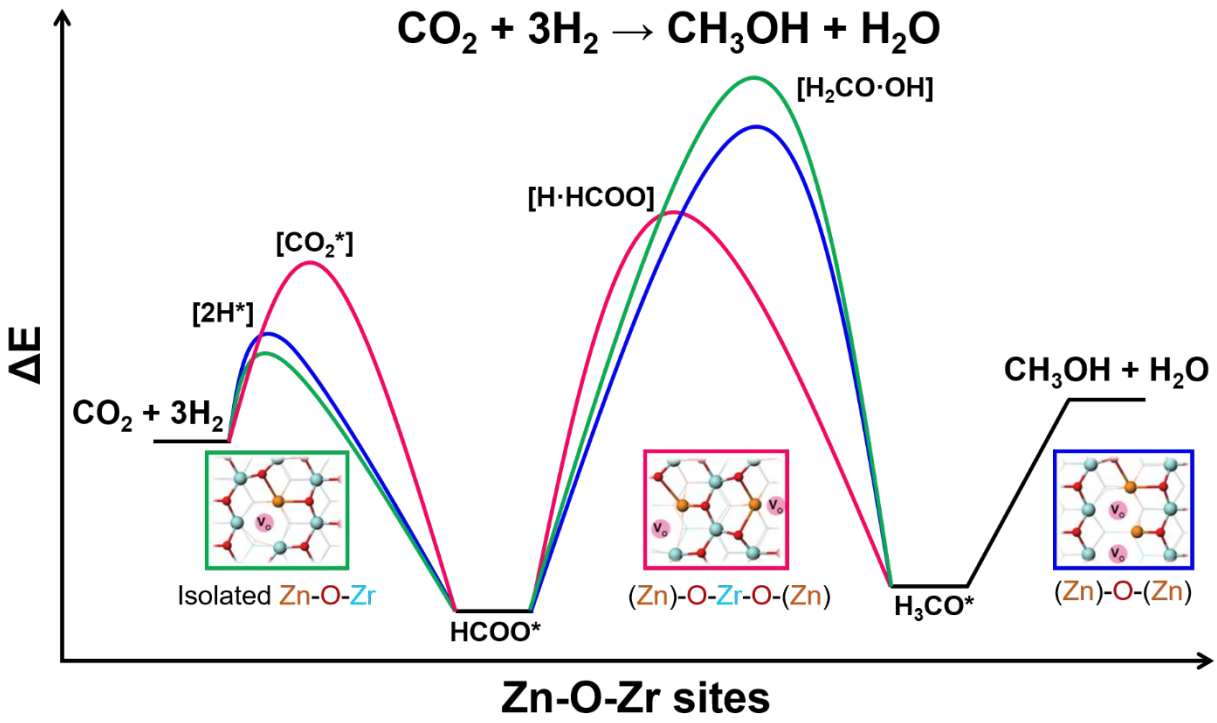

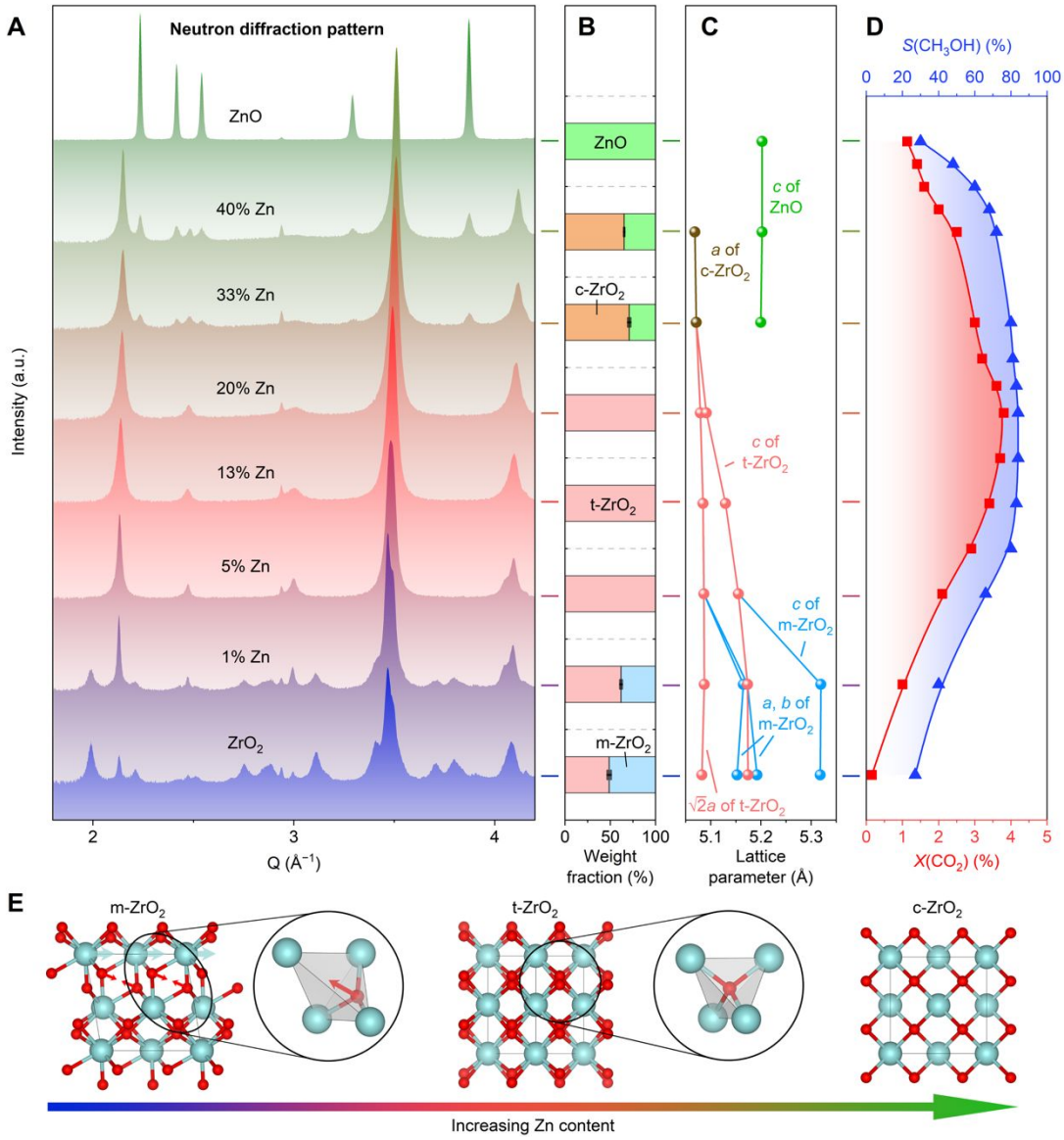

Figure 1. Crystal structures of ZnO-ZrO_2 solid solution catalysts and their catalytic performances. (**A**) The neutron diffraction patterns as a function of Zn content. (**B**) The weight fraction of different phases of ZrO_2. Monoclinic, tetragonal and cubic phases are denoted as m-ZrO_2, t-ZrO_2 and c-ZrO_2, respectively. (**C**) The variation of lattice parameters. (**D**) CO_2 conversion rate and selectivity of methanol product. Standard reaction conditions: 2.0 MPa, H_2/CO_2 = 3/1, 320 °C, GHSV = 24000 mL/(g h), using a tubular fixed bed reactor. (**E**) Evolution of crystal structure as a function of Zn content in ZnO-ZrO_2. Color code: Zr, cyan; O, red.

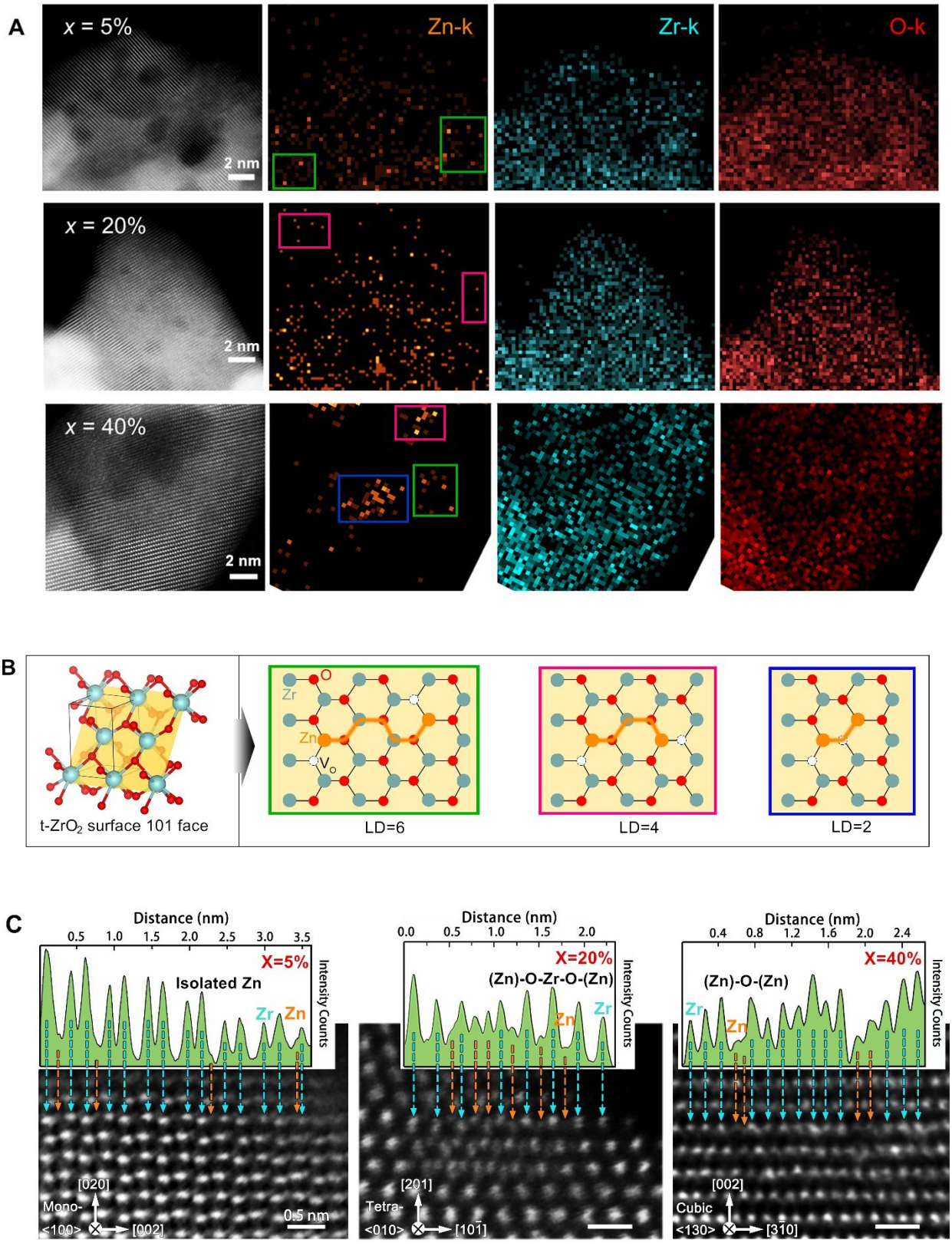

Figure 2. Characterization of coordination configurations near the surface. (**A**) Energy-dispersive spectroscopy (EDS) mappings of aberration-corrected scanning transmission electron microscopy (STEM) for 5%ZnO-ZrO_2, 20%ZnO-ZrO_2 and 40%ZnO-ZrO_2 samples. (**B**) Poroposed configurations with different link distance (LD) between Zn ions at t-ZrO_2 surface. Different colored borders correspond to areas in Figure 2A. Orange ball: Zn atom, Cyan ball: Zr atom; Red ball: O atom. (**C**) HAADF images of 5%ZnO-ZrO_2, 20%ZnO-ZrO_2 and 40%ZnO-ZrO_2 samples, the scale bars are all 0.5 nm.

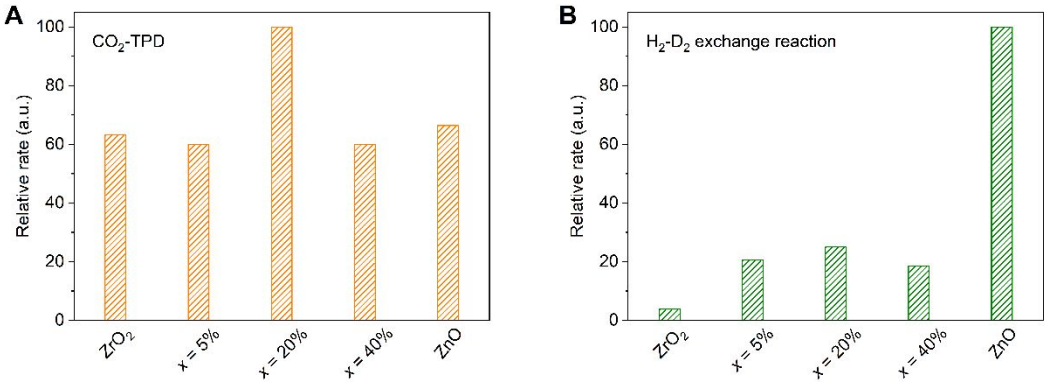

Figure 3. Activation of CO_2 and H_2 on ZnO-ZrO_2 solid solution catalysts. (**A**) CO_2-TPD on pure ZrO_2, ZnO and ZnO-ZrO_2 solid solution. (**B**) H_2–D_2 exchange reaction on pure ZrO_2, ZnO and ZnO-ZrO_2 solid solution.

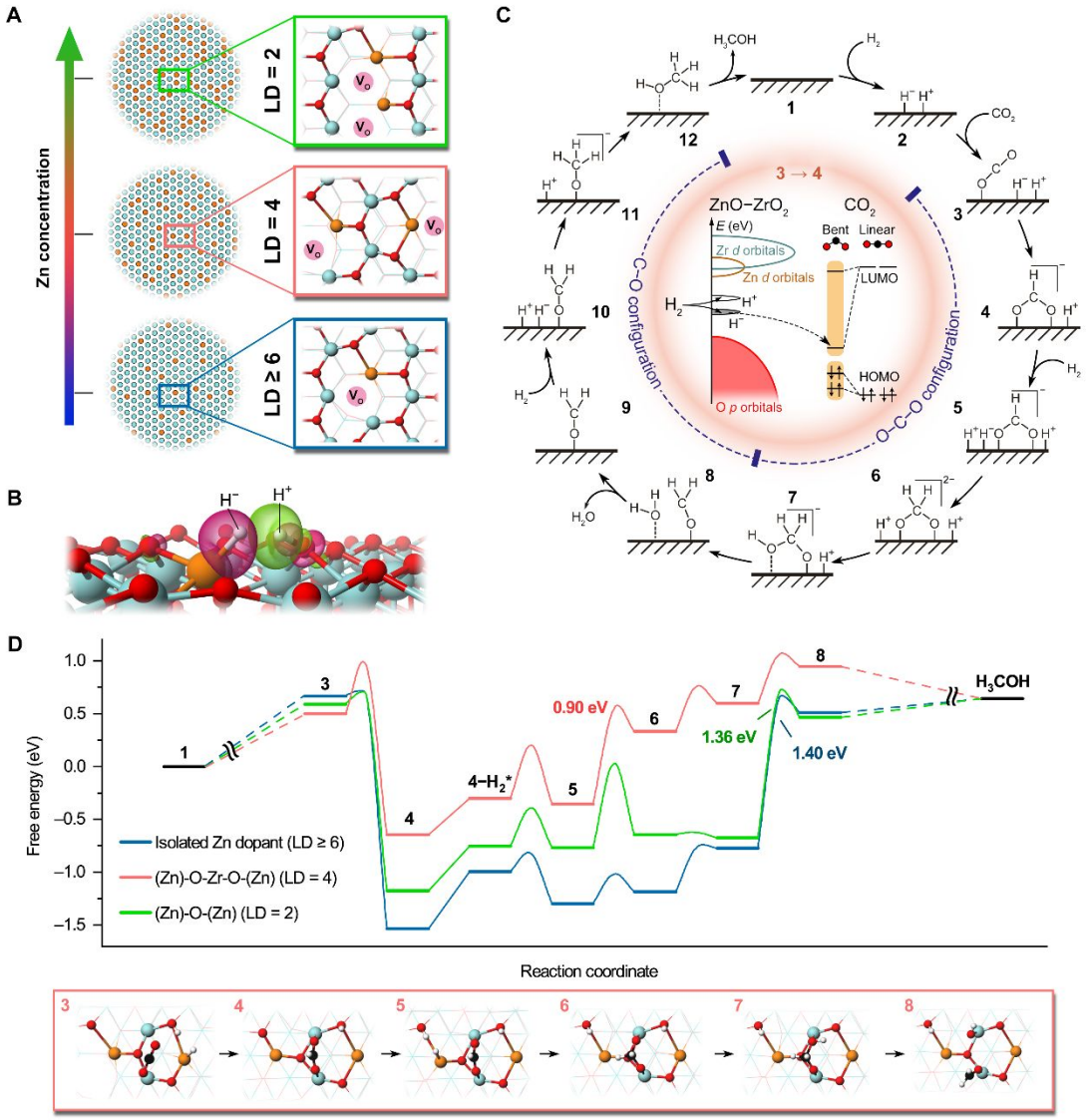

Figure 4. CO_2-to-methenal reaction mechanism on the catalytic sites with different coordination configurations at the surface. (**A**) Schematics of cation distributions on the (101) surfaces of the tetragonal ZnO-ZrO_2 catalysts with different Zn contents. The surfaces are featured by isolated Zn (LD ≥ 6), (Zn)-O-Zr-O-(Zn) (LD = 4) and (Zn)-O-(Zn) (LD = 2) coordination configurations. Only atoms in the surface layer are shown in spheres, while the structure beneath the surface is represented by wireframe. (**B**) Spatial distribution of charge density difference for the configuration after H_2 dissociation on Zn. Pink and green isosurfaces denote areas of charge accumulation and depletion (±0.05 e Å^{-3}), respectively, corresponding to the formation of H^- and H^+

ions. (**C**) Schematic reaction path, and an illustration of electron transfer in the first hydrogenation step (in the middle circle). The highest occupied molecular orbital (HOMO) and the lowest unoccupied molecular orbital (LUMO) of CO_2 are indicated, both consisting of the $2p_x$ and $2p_y$ orbitals. (**D**) The free-energy diagrams of methanol production at 593 K on isolated Zn, (Zn)-O-Zr-O-(Zn) and (Zn)-O-(Zn). The lower panel shows the atomic structures of the corresponding reaction intermediates. Color code: Zr, cyan; Zn, orange; O, red; C, black; H, white.

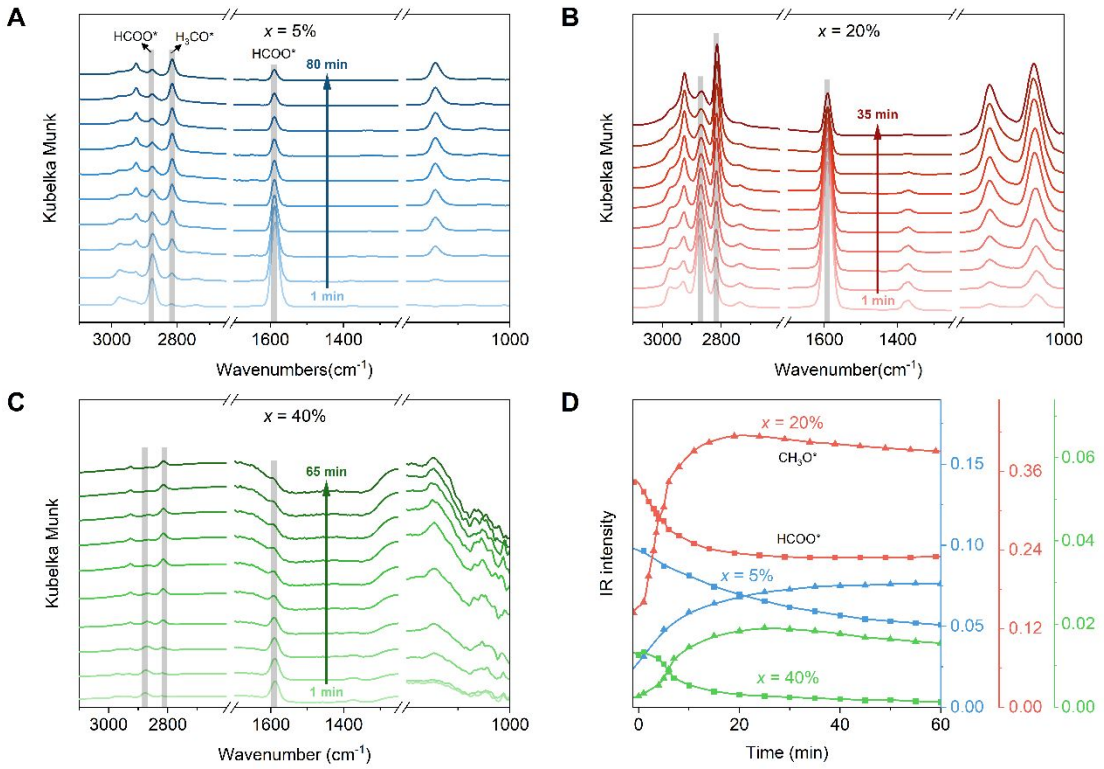

Figure 5. ***In-situ*** **DRIFT spectra of surface species**. (**A**) 5%ZnO-ZrO_2, (**B**) 20%ZnO-ZrO_2 and (**C**) 40%ZnO-ZrO_2. The gas is switched to H_2 for the catalysts with pre-adsorbed $CO_2 + H_2$. (**D**) The variation of surface species for the three ZnO-ZrO_2 catalysts.